Marine Geology 416 (2019) 105975

Contents lists available at ScienceDirect

Marine Geology

journal homepage: www.elsevier.com/locate/margo

Surface sediment composition and distribution of hydrothermal derived elements at the Duanqiao-1 hydrothermal field, Southwest Indian Ridge

Shili Liao[a,b,*], Chunhui Tao[a,b,h,*], Ágata Alveirinho Dias[c,f], Xin Su[d], Zhen Yang[e], Jianyu Ni[a,b], Jin Liang[a,b], Weifang Yang[a,b], Jia Liu[a,b], Wei Li[a,b], Chuanwan Dong[g]

[a] Second Institute of Oceanography, Ministry of Natural Resources, Hangzhou 310012, Zhejiang, China
[b] Key Laboratory of Submarine Geosciences, State Oceanic Administration, Hangzhou 310012, China
[c] Institute of Science and Environment, University of Saint Joseph, Macao
[d] School of Ocean Sciences, China University of Geosciences, Beijing 100083, China
[e] Faculty of Earth Resources, China University of Geosciences, Wuhan 430074, Hubei, China
[f] Instituto Don Luiz, Faculty of Sciences, University of Lisbon, Portugal
[g] School of Earth Sciences, Zhejiang University, Hangzhou 310027, China
[h] School of Oceanography, Shanghai Jiaotong University, Shanghai 200030, China

ARTICLE INFO

Editor: Gert J. De Lange

Keywords:
Sediments
Geochemistry
Duanqiao-1 hydrothermal field
Southwest Indian Ridge

ABSTRACT

The study of the hydrothermal component in oceanic sediments provides key data for locating active and inactive hydrothermal systems. In this work, we report the geochemistry of surface sediments collected in the newly discovered basaltic-hosted Duanqiao-1 hydrothermal field (DHF) on the Southwest Indian Ridge (SWIR). The sediments are mainly composed of a pelagic fraction (carbonate ooze) with minor clay contents, basaltic debris, Fe–Mn oxyhydroxides, and hydrothermal components. Hydrothermal elements in the DHF exhibit a precipitation sequence of Cu ≈ Co > Zn ≈ Pb > Fe > Mn ≈ Ni ≈ As. Proximal sediments to the hydrothermal discharge area are characterized by high Cu, Pb, Zn, and Co concentrations and higher Cu/Fe and Zn/Fe ratios, decreasing abruptly within the first kilometer. After this proximal area, an evident increase of Mn concentrations and Mn/Fe ratios was observed, denoting higher oxidizing conditions of the hydrothermal plume. Hydrothermal derived Pb and Co precipitated together with the sulfide phases, whereas at the distal sediments Pb, Co, Ni, and As seem to be scavenged from seawater by oxyhydroxides. This was corroborated by increased REE/Fe ratios with distance to the discharge zone. The geochemistry of DHF sediments is consistent with an effective separation of metals during gradual cooling, and concomitant Eh and pH modifications, of the hydrothermal plume when in contact with seawater. This promotes the precipitation of Cu sulfides first, closest to the discharge area, followed by Cu–Zn and Fe sulfides and Fe–Mn oxyhydroxides, in more distal areas. A comparison of the DHF sediments with those from Dragon Horn, another hydrothermal site at the SWIR, suggests that the hydrothermal fluids responsible for mineral precipitation at DHF are less reduced, favoring the formation of sulfides and oxyhydroxides at shorter distances from the discharge zone. These findings are particularly valuable to the understanding of the variation in hydrothermal anomalies detected in sediments from proximal and distal areas of discharge zones, contributing to the development of tools for the discovery of hydrothermal fields.

1. Introduction

Since the discovery of the first hydrothermal field (Corliss et al., 1979), scientific synergies have been put forward to increase the knowledge of seafloor hydrothermal processes. This is relevant both from a fundamental perspective, as it allows a better understanding of the importance of these systems in ocean chemistry, earth dynamics, and biological communities, but also from an applied standpoint, as declining metal resources on land makes deep-sea mining economically more viable. Seafloor massive sulfide (SMS) deposits are formed on and below the seabed via hydrothermal activity and are usually enriched in metals such as Cu, Pb, Zn, Au, Ag, and Co. The amount of these deposits is estimated to be in the order of 6×10^8 tons (Hannington et al., 2011). However, most of these estimates are based on known seafloor

* Corresponding authors at: Second Institute of Oceanography, Ministry of Natural Resources, Hangzhou 310012, Zhejiang, China.
E-mail addresses: yyxyzlsl@126.com (S. Liao), taochunhuimail@163.com (C. Tao).

https://doi.org/10.1016/j.margeo.2019.105975
Received 24 February 2019; Received in revised form 21 June 2019; Accepted 25 June 2019
Available online 04 July 2019

deposits and active hydrothermal systems that form buoyant plumes. Thus, to better estimate the dimension of seafloor deposits, an inventory of the inactive deposits is required.

Seafloor sediments adjacent to hydrothermal fields (HFs) are often affected by hydrothermal activities, acquiring mineralogical and chemical compositions distinct from the background sediments (Feely et al., 1987). Due to the long-term duration of hydrothermal activity, the geochemical features of sediments adjacent to HFs can provide information not only about the spatial distribution and intensity of the activity but also about the evolution and sedimentary flux of the field (Cave et al., 2002; Laurila et al., 2014). Therefore, investigating the geochemical features of seafloor sediments can help to identify both active and ancient hydrothermal fields.

There are several geochemical and mineralogical methods to identify hydrothermal signatures in sediments (e.g., Boström et al., 1969; German et al., 1999; Hrischeva and Scott, 2007; Huang et al., 2017; Pan et al., 2018) and, with the discovery of ultramafic-hosted hydrothermal vent fields, new approaches were added. The chemical composition and spatial distribution of hydrothermal-derived elements around ultramafic-hosted HFs are considerably different than those from volcanic-related HFs (e.g., Mottl and Mcconachy, 1990; Cave et al., 2002; Edmonds and German, 2004; Coogan et al., 2017; Dias et al., 2010). For example, sediments from ultramafic-hosted HFs are usually richer in ultramafic-derived elements, such as Mg, Ni, and Cr (Kuhn et al., 2000; Yu et al., 2018; Dias et al., 2010), and metalliferous sediments and deposits typically exhibit high Cu and Co contents and high Cu/Fe values (Cave et al., 2002; Dias and Barriga, 2006; Rusakov et al., 2013; Yang et al., 2016b).

The ultraslow-spreading Southwest Indian Ridge (SWIR) is characterized by limited magma supply and was thought to be lacking hydrothermal activity (Baker et al., 2004). However, after the discovery of the first active HF (Longqi-1) in 2007, more HFs have been observed in this area, including the Duanqiao-1, Yuhuang-1, Longqi-3, Junhui-1, Tiancheng-1, Tianzuo-1, and Changbai-1 fields (Tao et al., 2012, 2014). These discoveries imply abundant hydrothermal activity on the SWIR. Currently, at least two types of sulfide mineralization have been identified on the SWIR: (1) the Duanqiao-1 HF (DHF) located on-axis under volcanic settings (Yang et al., 2016a) and (2) the Longqi-1 HF located off-axis, near an oceanic core complex (OCC), at the hanging wall of a detachment fault (Zhao et al., 2013; Tao et al., 2014; Liang et al., 2014). The distribution of hydrothermal elements in the Dragon Horn area, where the Longqi-1 HF is located, has been previously characterized (Liao et al., 2018).

Here, we present the geochemical characterization of DHF sediments to evaluate possible geochemical anomalies related to the nearby hydrothermal system. We compare these results with those from the Dragon Horn area in relation to the spatial zonation of hydrothermal elements within surface sediments and the mechanisms that form the patterns of zonation. This study can be particularly valuable to the understanding of the variation in the hydrothermal anomalies detected in sediments from proximal and distal areas of the discharge zone, contributing to the development of valuable tools for the discovery of HFs.

2. Geological background

The study area is located at the shallowest zone of the ultraslow-spreading SWIR (Dick et al., 2003), between Indomed and Gallieni transform faults. It is positioned at an axial highland (central volcano) in the shallow portion (~1700 m water depth) of segment 27 (72 km long; Cannat et al., 1999; Tao et al., 2012). The ridge volcanic axis (RVA) is developed without obvious ridge rift (Fig. 1). Beneath segment 27, the oceanic crust is unusually thick (~10 km), which is probably related to the existence of a well-developed magma chamber (Sauter et al., 2004; Li et al., 2015; Niu et al., 2015; Jian et al., 2017). Most of the study area is covered by pillow basalt or basaltic debris with sediments covering the depressions. The sediments are described as calcareous shell remains of foraminifera (oozes) with a low content of pelagic clays and lithogenic detritus (Chen et al., 2013). The DHF was discovered during the DY115-20 cruise. Massive sulfide deposits, sediments, and opal samples were collected using TV-Grab. Focused turbidity, temperature, and methane anomalies were not observed using tow-yo or CTD investigations (Tao et al., 2014). The dating of DHF sulfide chimneys using $^{230}Th/^{238}U$ ratios revealed that this field suffered several episodes of hydrothermal activity distributed between 0.737 and 84.338 kyrs ago (Yang et al., 2016a). Although no plume signals were detected, locally hydrothermal diffuse venting was observed by HOV survey (Shenhaiyongshi by RV Tansuoyihao) during the 2018–2019 cruise on SWIR. In situ temperature measurements of the venting fluid revealed values as high as 277 °C. Those observations indicate that DHF is still partially active at local area.

3. Sampling and analysis methods

3.1. Sampling

Surface sediments were sampled using a TV-Grab and a multi-tube sampler on six cruises, DY115–20, 21, DY125-30, 34, 40, and DY135-49, conducted between 2008 and 2018. Areas with a thicker sediment cover were chosen for sampling, in particular the western portion of the field, because the bottom current activity is mainly directed northwest (Liao et al., 2015). Approximately the upper 10 cm of the sediment samples was analyzed based on: (1) The age of this layer is estimated at 10 ka according to previous studies that show a sedimentation rate of the SWIR of ~1 cm/kyr (Mcarthur and Elderfield, 1977), which may increase to 2.7–3.8 cm/kyr in the vicinity of HFs (Daessle et al., 2000; Cave et al., 2002), and (2) that the field was active 0.737 (± 0.023) kyrs ago (Yang et al., 2016a).

Twenty-four surface sediments were collected (Fig. 1 and Appendix 1) at a water depth ranging from 1653 to 2456 m. Additionally, four samples were collected along the ridge flank located > 60 km away from the ridge axis to represent the mineral composition and geochemistry of the background sediments. These sediments were characterized by pale brown to white carbonate oozes and basaltic debris (< 1%). The X-ray diffraction phase analysis suggested that the sediments were mainly comprised of calcite (> 95%), with minor quartz (< 1%), aragonite (1%–5%), and clay minerals (mainly kaolinite, about 2%; Chen et al., 2013).

3.2. Analytical methods

Geochemical analyses were performed at the ALS Laboratory Group in Guangzhou, China. Before analyses, samples were dried and sieved using a 60-mesh (250 μm) standard sieve to reduce the influence of debris on sediment composition (Liao et al., 2017). Major elements were analyzed using X-ray fluorescence spectrometry (PANalytical PW2424). Prior to analysis, each sample was fully mixed with a flux containing lithium nitrate and heated at 1000 °C for ~1 h. After melting, each sample was transferred into a platinum mold to form a flat glass sheet. Three standard samples (GBW07105, NCSDC47009, and SARM-4) were used during the analyses to monitor data accuracy. The measurement error for the collected data was within 5%.

Trace elements were analyzed using an Agilent 7700x ICP-MS. Sediment samples were crushed to grains < 74 μm (200 mesh) in an agate mortar. Then, ~250 mg of each sample was weighed and digested with $HClO_4$, HNO_3, and HF. The solutions were evaporated until dry; the residue was leached and dissolved using diluted HCl, and the dissolved sample was analyzed. The results were corrected for spectral inter-element interferences. Reference samples GBM908–10 and MRGeo08 were used as internal standards for data quality control. The measurement error on the data was within 10%.

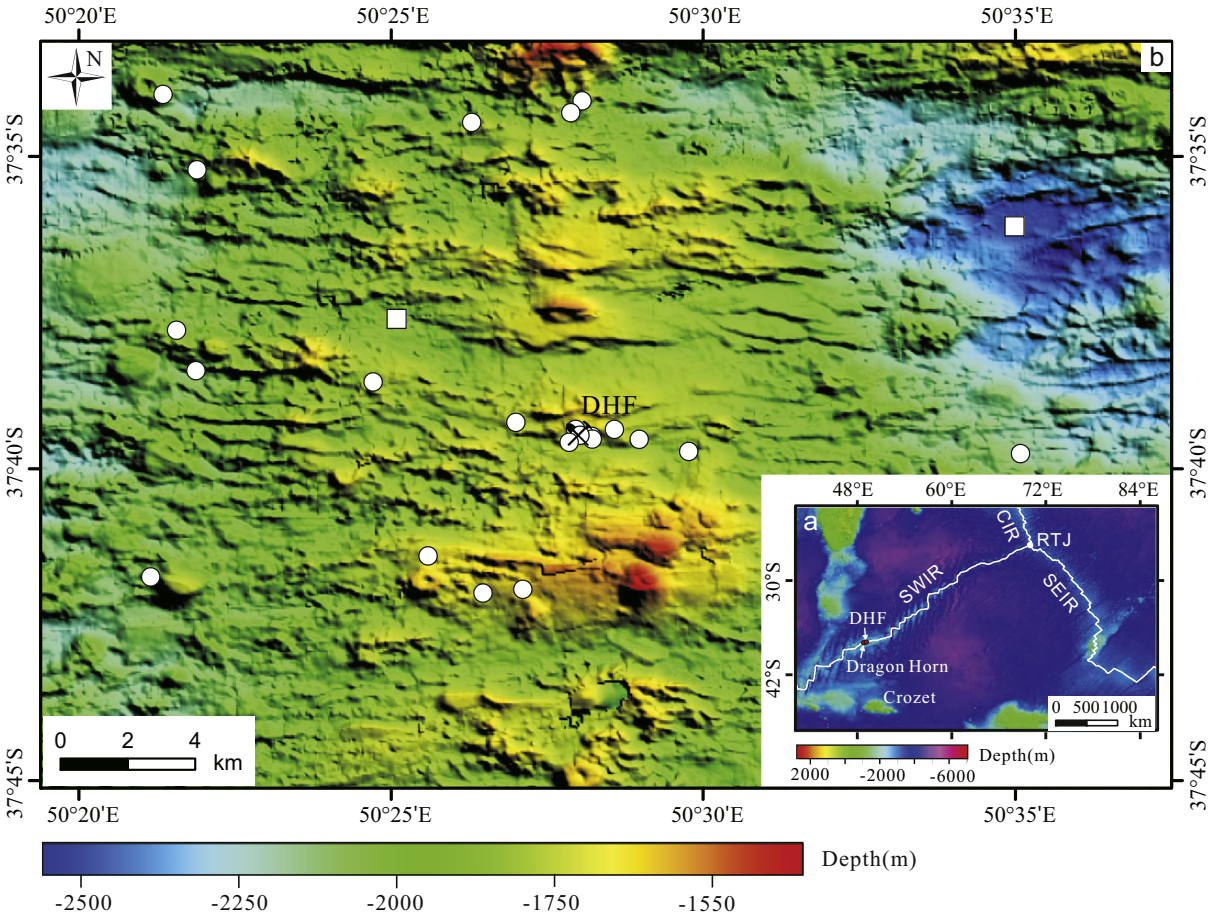

Fig. 1. Location and topography of the study area. White points and squares are sediments sampled using TV-Grab and a multi-tube sampler, respectively. Topography data were obtained from the General Bathymetric Chart of the Oceans (GEBCO, 2008) and multibeam bathymetry studies.

4. Results

The statistic results of the sediments are shown in Table 1. Full geochemical results are given in Appendix 1.

4.1. Major elements

Whole geochemical analyses show that the DHF sediments exhibit CaO content ranging from 45.10 to 52.87 wt% (average = 50.25 wt%), which is comparable to background sediments (BGS: average = 50.97 wt%) (Appendix 1). The contents of Al_2O_3, TFe_2O_3, and MgO are 0.50–2.83, 0.39–2.16, and 0.27–1.25 wt%, with average values of 1.22, 0.99, and 0.53 wt%, respectively, which are higher than those of background sediments. Compared with background sediments, the DHF sediments also exhibit higher SiO_2 and TiO_2 content with average values of 1.73–9.17 and 0.02–0.22 wt%, respectively. As Al and Ti are relatively immobile elements in MOR hydrothermal systems (e.g., Boström, 1973; Dias and Barriga, 2006), they may represent clastic/detrital components in sediments and, accordingly, their levels were high in the DHF samples (average Al = 0.79 wt% and Ti = 0.06 wt%). As the BGS were collected at the ridge flanks, these elements also show higher levels of clastic/detrital components within the ridge axis sediments compared with the ridge-flank sediments, which is similar to the sediment features near the Rodrigues Triple Junction on Central Indian Ocean (Kuhn et al., 2000).

4.2. Trace elements

Copper and Zn contents range from 9.4 to 338 ppm and from 10 to 105 ppm with averages of 57.9 and 31.8 ppm, respectively. The Pb content ranges from 2.7 to 27 ppm (Pb_{median} = 9.55 ppm). The content of Pb, especially in the proximal sediments, is considerably higher than in the background (Pb = 4.7 ppm) and the metalliferous sediments (Pb = 4.2 ppm) from Dragon Horn area. Metals, such as Cu, Pb, Zn, Fe, Mn, Co, and As, have significantly higher concentrations in the DHF than in the background sediments (Table 1). In addition, the average Cu/Al, Zn/Al, and Pb/Al ratios of the DHF sediments (79.13, 48.21, and 16.26, respectively) are higher than those of background sediments (42.11, 33.24, 10.96, respectively), indicating that the enrichment of these elements in the sediments possibly results from a contribution by hydrothermal components. The average Ni and Cr contents are 11 and 10 ppm, respectively, almost similar to the background sediments (Ni = 14 and Cr = 6 ppm), but lower than the sediments from Dragon Horn area (28 and 27 ppm, respectively).

4.3. Rare earth elements and yttrium (REY)

REY concentrations were normalized to the chondrite values (Taylor and Mclennan, 1985). The deviations of Eu and Ce from their neighbors lanthanide elements were defined by Eu and Ce anomalies [$Eu/Eu^* = 2(Eu/Eu_n)/(Sm/Sm_n + Gd/Gd_n)$; $Ce/Ce^* = 2(Ce/Ce_n)/(La/La_n + Pr/Pr_n)$; Table 1]. Sediments from DHF exhibited ΣREE contents ranging from 19.91 to 59.75 ppm, and chondrite-normalized REY distribution patterns show a strong enrichment in LREE (Fig. 2a) with LREE/HREE values between 1.15 and 2.01. All sediment samples show negative Eu anomalies (Eu/Eu^* = 0.60–0.80; average 0.71). Negative Ce anomalies (Ce/Ce^* = 0.52–0.94; average 0.72) were also present in the majority of the sediments, except for two sediment samples that

Table 1
Major and trace elements of the sediments from the DHF and comparison with the Dragon Horn area.

Elements	DHF sediments					BGS (n = 4)	Dragon Horn metalliferous sediments (n = 8)	Dragon Horn non-metalliferous sediments (n = 47)	Basalt (n = 26)	Serpentinite (n = 19)	CIR sediments
	Min	Max	Average	Median	SD	Average	Average	Average	Average	Average	Average
$CaCO_3$ (wt%)	80.49	94.36	89.68	89.62	3.39	90.97	83.01	85.35	20.09	1.45	
SiO_2 (wt%)	1.73	9.17	3.94	3.69	1.85	3.12	7.14	6.25	48.95	41.10	12.75
Al_2O_3 (wt%)	0.50	2.83	1.22	1.12	0.59	0.81	1.31	1.74	16.16	1.56	2.55
TFe_2O_3 (wt%)	0.39	2.16	0.99	0.83	0.54	0.55	2.44	1.33	11.10	8.57	2.29
K_2O (wt%)	0.09	0.21	0.14	0.13	0.03	0.77	0.17	0.22	0.14	0.02	
MgO (wt%)	0.27	1.25	0.53	0.48	0.24	0.38	1.77	0.99	8.38	36.17	0.84
Na_2O (wt%)	0.61	1.58	1.03	1.02	0.23	1.24	1.06	1.21	2.39	0.10	0.96
MnO (wt%)	0.02	0.12	0.06	0.065	0.03	0.04	0.08	0.05	0.16	0.12	
P_2O_5 (wt%)	0.01	0.09	0.05	0.05	0.02	0.06	0.06	0.06	0.06	0.03	0.07
TiO_2 (wt%)	0.02	0.22	0.08	0.06	0.05	0.04	0.08	0.09	1.10	0.03	0.04
LOI (wt%)	37.34	44.91	41.95	42.46	1.73	43.12	39.67	40.62	0.05	11.71	
Mo (ppm)	0.14	0.97	0.42	0.35	0.24	0.4	1.53	0.33	0.09		
Bi (ppm)	0.05	0.17	0.08	0.08	0.03	0.06	0.11	0.07	0.02		
Cu (ppm)	9.4	338.0	57.9	23.85	79.35	18.1	333.2	47	93	15	141
Pb (ppm)	2.7	27.0	10.5	9.55	7.17	4.7	4.2	5	2	1	20
Zn (ppm)	10	105	31.8	24.00	25.99	14.3	50	24	95	32	83
As (ppm)	3	8	4	4.10	1.60	1.9	6	3	1		5
Sb (ppm)	0.00	0.32	0.16	0.14	0.08	0.15	0.21	0.15			
Co (ppm)	5	22	12	11.65	5.29	7	17	8	49	85	24
Ni (ppm)	6	20	11	9.50	4.02	14	56	24	143	1515	110
Cr (ppm)	3	27	10	9.00	6.36	6	40	25	230	1530	30
V (ppm)	4	42	17	13.00	11.28	6	26	20	270	30	22
Ti (ppm)	0.02	0.13	0.05	0.05	0.03	0.026	0.05	0.054			
Mn (ppm)	173	956	468.25	465.00	221.73	305	536	401			2600
MSI	38.01	57.20	47.31	47.73	4.88	50.97	33.41	48.38			
ΣREE	19.91	59.75	31.32	29.80	8.12	43.37	33.48	41.66			
LREE	11.81	39.27	18.87	18.40	5.36	25.67	19.66	24.58			
LREE	6.62	20.48	12.45	11.92	3.12	17.7	13.82	17.08			
L/H	1.15	2.01	1.53	1.48	0.22	1.46	1.43	1.46			
$(Eu/Eu^*)_N$	0.60	0.80	0.71	0.73	0.06	0.71	0.7	0.72			
$(Ce/Ce^*)_N$	0.52	1.31	0.76	0.74	0.20	0.57	0.63	0.58			

Note: MSI is the "Metalliferous Sediment Index" given by 100*Al/(Al + Fe + Mn) values (Boström et al., 1969). L/H is the ratio between LREE/HREE. Data from Dragon Horn area are from Liao et al. (2018); Basalt and serpentinites were partially published by Yang et al. (2017) and Chen et al. (2015). Central Indian ridge sediments (CIR) are from Kuhn et al. (2000).

exhibited significant positive Ce anomalies (40I-TVG02 = 1.20 and 34III-TVG07 = 1.31). Sediments were also normalized to the background sediments (BGS; Fig. 2b) to evaluate the major differences on the REY contents relatively to pelagic sediments without hydrothermal signatures. Although the sediments from DHF exhibit REY patterns similar to BGS patterns, they are slightly enriched in HREE. Major differences can be also observed in the Eu and Ce anomalies. Positive Eu anomalies are more evident in proximal sediments and sometimes are associated with less negative or even slightly positive Ce anomalies (Fig. 3). These positive anomalies observed in the BGS-normalized patterns corroborates a stronger hydrothermal signature in the area near the discharge zone.

5. Discussion

5.1. Sediment composition

To better understand the contribution of the hydrothermal-derived elements in the surface sediments from DHF, a comparison to the BGS was performed. The BGS are pelagic sediments characterized by Liao et al. (2018) as calcareous oozes mixed with basaltic debris and Fe–Mn oxyhydroxides (hereafter referred to as Fe–Mn oxides; Table 1 and Appendix 1). In the DHF, the calculated $CaCO_3$ content of the sediments show values usually higher than 90%, which is in agreement with the main composition of the BGS. However, the contribution of basement-derived debris and hydrothermal-derived signatures in the sediments is evident. On the Al_2O_3–TiO_2 and Al_2O_3–MgO diagrams, surface

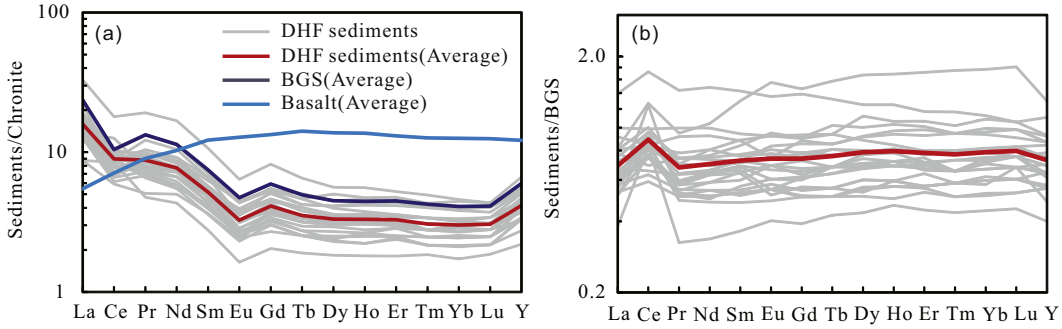

Fig. 2. REY patterns of the DHF sediments normalized to (a) chondrite (Taylor and Mclennan, 1985) and to (b) background sediments (BGS).

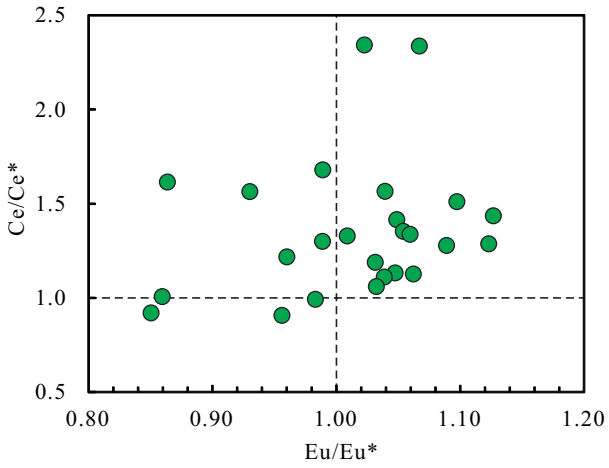

Fig. 3. BGS normalized Eu/Eu* vs Ce/Ce* diagram of the DHF sediments.

sediments from the DHF plot between the background sediments and basalts (Fig. 4a and b), indicating that they contain minor basaltic debris. This result is different for surface sediments from the Dragon Horn area, Rainbow, and Saldanha that contain significant ultramafic debris (Cave et al., 2002; Dias and Barriga, 2006; Liao et al., 2018), as supported by a high content of MgO (Fig. 4b). In addition, sediments from the DHF exhibit lower Al and Mg contents compared with those from the CIR and Endeavor Ridge Segment (Fig. 4b), indicating a lower basaltic debris content in the sediments from the study area (Kuhn et al., 2000; German, 2003).

Sediments in the DHF exhibit a clear enrichment in metals, such as Cu, Zn, Pb, Fe, and Mn (Fig. 5a and b), suggesting the input of hydrothermal-derived elements. As no apparent sulfide debris was found in the sediments, the high content of these elements is likely driven by hydrothermal fallout or directly precipitated within the sediment during the rise of the fluid. This is also consistent with previously results showing that indexes of Fe, Cu, and Zn content are sufficiently sensitive to differentiate the effects of diverse hydrothermal activities on surface deposits in the SWIR (Pan et al., 2018). In addition, the DHF sediments exhibit a Fe–Cu-enrichment pattern, similar to the Dragon Horn and Endeavor field (Fig. 5b). Most of the Saldanha sediments, in comparison with the ones of the DHF, have a higher content of Fe—Mn oxyhydroxides (Fig. 5a) and sulfides dominated by Zn-rich sulfide phases (Fig. 5b), typical from low-temperature hydrothermal activity (Dias and Barriga, 2006). Surprisingly, the DHF sediments exhibit higher Pb content than the Dragon Horn area and background sediments (Fig. 6), even similar to the pattern of sediments influenced HFs (e.g., Jan Mayen and Loki's Castle; Baumberger et al., 2016; Cruz, 2016). It has been reported that sulfide developed on sediment-starving mid-ocean ridges exhibit low Pb contents (Hannington et al., 2005). We propose that the hydrothermal plume inherited the Pb enrichment feature from the DHF vent fluid, which is supported by the Pb-rich features of the sulfide recovered from this field (Yang, 2017). Pb was scavenged by the Fe—Mn oxyhydroxides in the hydrothermal plume, that later precipitated within the sediment cover. This hypothesis is well supported by the strong positive correlation between Pb and Mn (Fig. 6, Pearson's correlation, $R = 0.827$; $P = 0.000$; $N = 24$). Additionally, Pb can be also derived from the hydrothermal fluid and incorporated in the plume sulfide minerals that have precipitated within the sediment.

To differentiate the pelagic sediments with and without metalliferous/hydrothermal inputs, the "Metalliferous Sediment Index" (MSI; 100*Al/(Al + Fe + Mn); Boström et al., 1969) was used. Index values < 40% or 60% have been previously interpreted as demonstrating abundant hydrothermal input to ridge-flank sediments (e.g., Yamamoto, 1987; German, 2003; Dias and Barriga, 2006; Du et al., 2007; Hung et al., 2018). The DHF sediments show MSI values below 60%, with 17 samples below 50% as with a minimum value of 38.01% (Table 1), indicating a slight enrichment in metalliferous contents in some of the sediments.

On the Si–Fe–10 Mn diagram, most of the sediment samples from the DHF plot between basalt and the background sediments (Fig. 5a). Some samples plot closer to the Fe—Mn oxide region, suggesting that they contain significant Fe—Mn oxides. However, the DHF sediments show relatively higher Mn content compared with the ones from Dragon Horn (Figs. 5a and 6). This suggests that oxides from DHF are dominantly Mn-rich phases, in contrast with the ones from Dragon Horn that are dominantly Fe-rich phases. In addition, Fe—Mn oxides of hydrothermal origin generally display chondrite-normalized REY patterns with negative or no Ce anomalies, whereas hydrogenetic Fe—Mn oxides are typically characterized by positive Ce anomalies due to the oxidative scavenging of Ce from seawater (Elderfield et al., 1981; Kuhn et al., 1998). Further, seafloor oxidation processes of the basaltic debris of the sediments may produce negative Ce anomalies (Ludden and Thompson, 1979). Compared with the background sediments, sediments in the DHF exhibit positive $Ce/Ce^{*}_{(BGS\ normalized)}$ anomalies, showing extremely high values in two samples (Fig. 3). Therefore, part of the Fe—Mn oxides of the sediments is probably hydrogenetic.

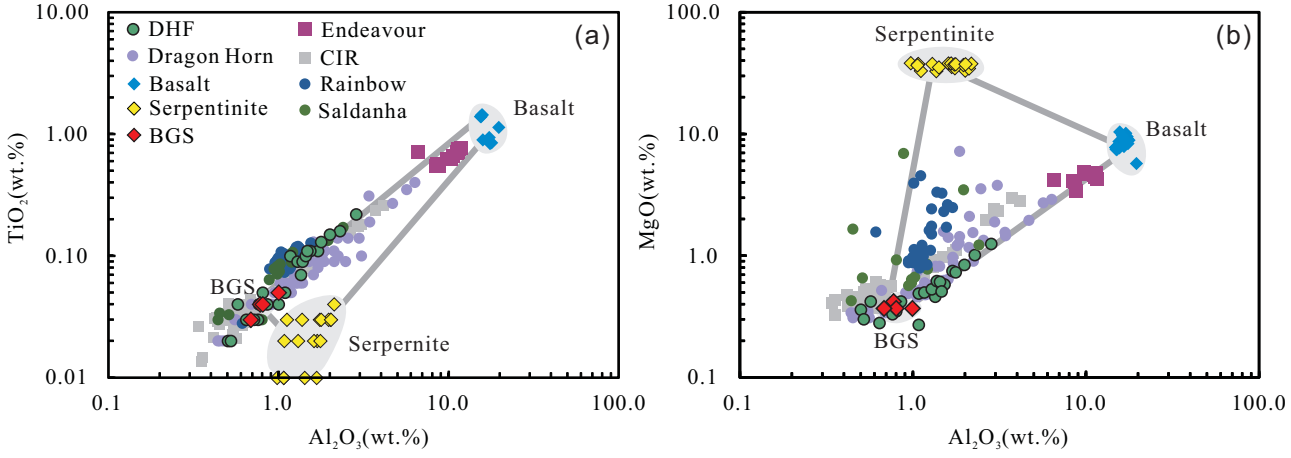

Fig. 4. Diagrams of Al_2O_3–TiO_2 (a) and Al_2O_3–MgO (b) for the DHF (Duanqiao-1). For comparison, data from background sediments (BGS); Dragon Horn (Liao et al., 2018); Endeavor HF (Hrischeva and Scott, 2007); CIR (Kuhn et al., 2000); Rainbow HF (Cave et al., 2002; Chavagnac et al., 2005; Dias and Barriga, 2006); Saldanha (Dias and Barriga, 2006); Basalt (Yang et al., 2017) and Serpentinite (Chen et al., 2015) are also plotted.

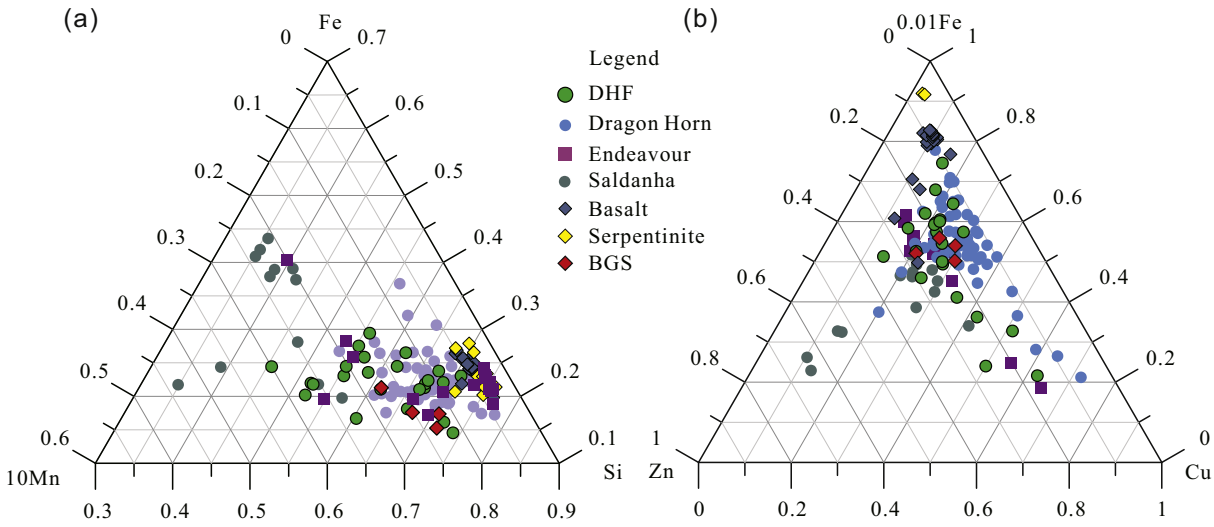

Fig. 5. Si–Fe–10Mn (a) and 10Cu–0.1Fe–Mn (b) diagrams of sediments from the DHF. For comparison, data from others sources is plotted. Data base: background sediments (BGS) and Dragon Horn (Liao et al., 2018); Endeavor (Hrischeva and Scott, 2007); Saldanha (Dias and Barriga, 2006); Basalt (Yang et al., 2017); Serpentinite (Chen et al., 2015).

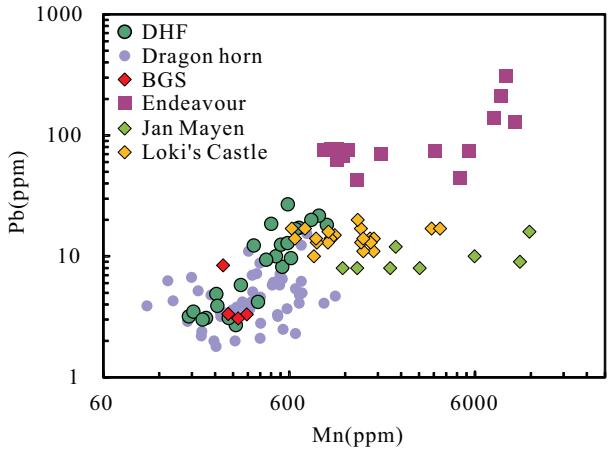

Fig. 6. Comparison of Pb and Mn content of sediments from the DHF and Dragon Horn area. For comparison, data from others sources is plotted. Data base: background sediments (BGS) and Dragon Horn (Liao et al., 2018); Endeavor HF (Hrischeva and Scott, 2007); Jan Mayen and Loki's Castle (Cruz, 2016).

5.2. Distribution and zonation of hydrothermal elements

In order to identify the hydrothermal fluids-derived elements and the ones that were scavenged from seawater by the hydrothermal buoyant plumes, the hydrothermal origin of elements was calculated according to the formulas suggested by Cave et al. (2002) and Liao et al. (2018): $Element_{Hydrothermal} = Element_{Total} - Element_{Basaltic}$ (see Supplementary Methods for details). Concentrations of these elements with distance to the hydrothermal field were analyzed to understand if there was any pattern in the dispersal features of hydrothermal-derived elements (Fig. 7). Further, to better identify the proportion of the different elements in the whole sediment, element/Fe ratios were also studied (Fig. 8).

5.2.1. Cu, Pb, Zn, Co, Fe, and Mn

The results show a clear enrichment in Cu, Zn, and Fe near the source, decreasing abruptly within the first kilometer and maintaining very low concentrations after that (Figs. 7a and d). The same was visible for the Cu/Fe, Zn/Fe ratios, which decrease with increasing distance to the DHF (Fig. 8a). Contrarily, Mn shows higher concentrations between the 2nd and 7th km (Fig. 7c). These results put in evidence an effective separation of Cu, Zn, and Fe in the fluids relatively to Mn. This is a consequence of the chemico-physical conditions of the fluid when the mixing with the bottom seawater occurs. Due to the decrease in temperature and Eh and increase in pH conditions, occurring when the buoyant plume moves away from the source and undergoes greater interaction with the bottom seawater, the Cu–Zn–Fe–sulfides precipitate first, near the source. The Fe and Mn are transported beyond the discharge zone and dispersed in the open ocean, precipitating as oxyhydroxides in more distant zones. The effective separation of these metals is also corroborated by the decreasing ratios of Cu/Fe and Zn/Fe and increasing ratio of Mn/Fe with the distance to the discharge zone.

Although hydrothermal-derived Cu and Zn exhibit similar dispersal distances (Fig. 7a), the Cu/Fe values show a slightly faster decrease relatively to the background values than the Zn/Fe ratio, with values starting to decay at a distance of 1.0–1.5 and 1.5–2 km from the source (Fig. 8a), respectively. This suggests that Cu-rich sulfides precipitated before more intense mixing processes occurred within the plume, followed by the precipitation of Zn-rich sulfides.

The distribution of Pb and Co is similar to that of Cu, Zn, and Fe within the first kilometer but shows a second peak between the 3rd and 9th kilometer (Figs. 7b and 8b). This indicates that Pb and Co were incorporated in the sulfide structures in the early stage of plume formation. The second enrichment is explained by the scavenging of those elements from the seawater by oxyhydroxides, which takes place due to the continuous mixing processes of the hydrothermal plume with seawater. The relationship between those elements is also supported by the high correlation of Co with Mn ($r = 0.892$; $P = 0.000$; $N = 24$). Further, sediment samples collected 2 km away from the DHF exhibit higher correlations of Pb with Mn ($r = 0.903$; P = 0.000; $N = 16$) than total samples ($r = 0.827$; P = 0.000; N = 24), indicating that Pb and Co were absorbed to oxyhydroxides after the majority of sulfides have been precipitated.

5.2.2. Ni, As

Hydrothermal Ni, As, and the Ni/Fe and As/Fe values increased with increasing distance from the DHF, with maximum values at ~10 km and decreasing values beyond that distance (Figs. 7c, d and 8c, d). This feature is similar to the distribution of Mn and is consistent with former studies (e.g., Feely et al., 1991; Edmonds and German,

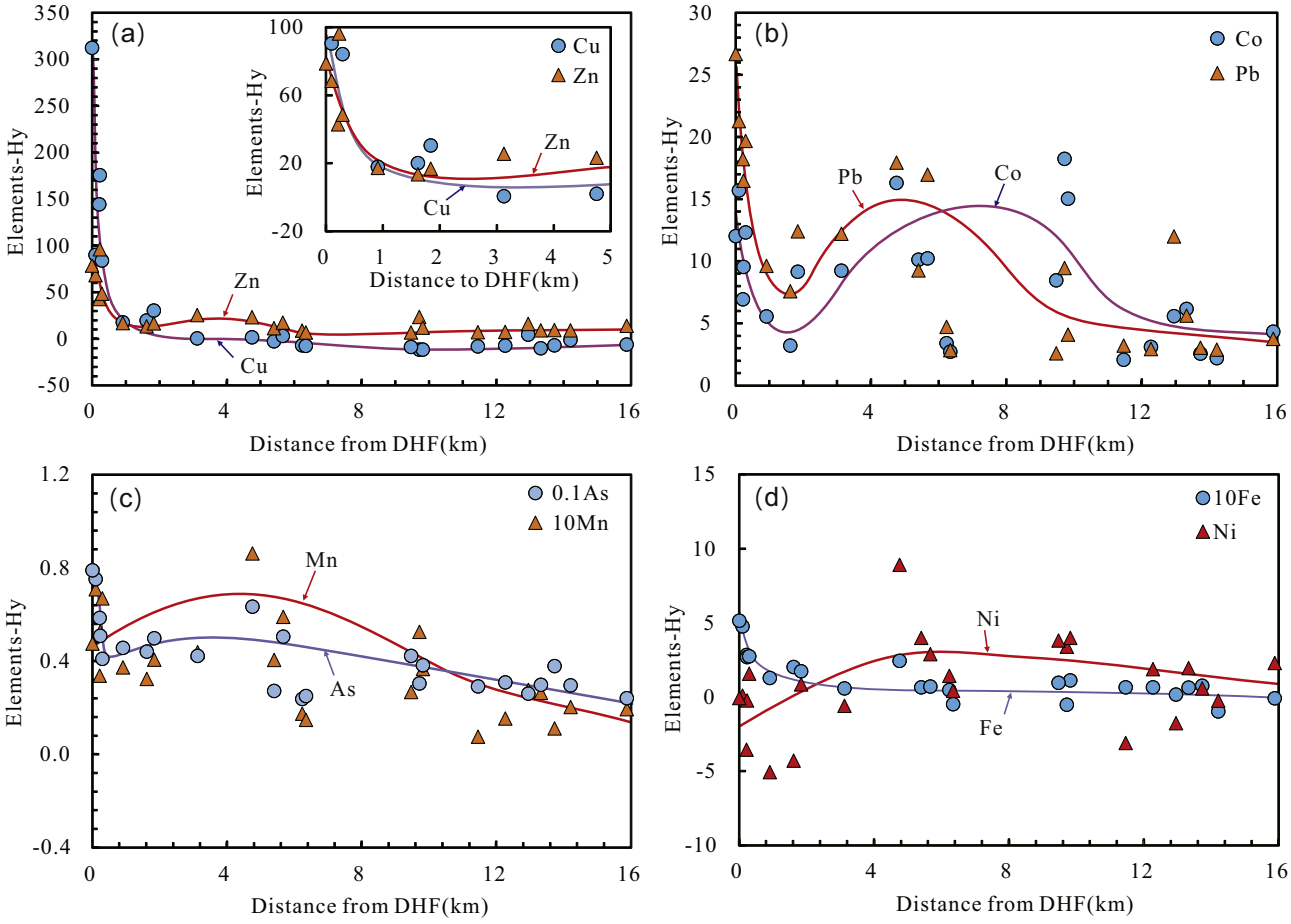

Fig. 7. Hydrothermal elements in sediments with increasing distances from the DHF. (a) Cu and Zn; (b) Co and Pb; (c) As and Mn; (d) Fe and Ni. Note: Hydrothermal derived elements were calculated according to Cave et al. (2002) and Liao et al. (2018) by formula $Element_{Hydrothermal} = Element_{Total} - Element_{Basaltic}$. The details of the process have been provided in Supplementary Methods. Fe and Mn were minus 10 times while As were divided 10 times to be shown on the same scale. Data with negative values represent no hydrothermal elements input or values below the background value. The unit for Fe and Mn were wt%, whereas the others were ppm.

2004; Coogan et al., 2017), indicating that these hydrothermal elements are mainly incorporated via scavenging processes by the oxyhydroxides.

5.2.3. Rare earth elements

The initial REY pattern of the hydrothermal fluid is also continuously modified during the dispersal of the hydrothermal plume due to physic-chemical changes related with the increasing dilution of the fluid by unmodified seawater (Zeng et al., 2015). The REY patterns from plumes become overprinted by those of seawater due to the scavenging of REE by oxyhydroxides from seawater, which later precipitate in more distal sediments, explaining the higher ratios of ΣREE/Fe and ΣREE/Mn in distal zones of the field (Fig. 9a). In agreement, the sediments collected at higher distances to the hydrothermal source show lower negative BGS-normalized Ce anomalies (Fig. 9b), consistent with the fallout from neutrally buoyant plumes due to the absorption of REY from seawater by Fe oxide particles during plume dispersal. The $Eu/Eu^{*}_{(BGS\ normalized)}$ anomalies are not related to distance from the DHF.

5.3. Factors controlling the dispersal of hydrothermal elements within the DHF

The DHF is located ~60 km away from the Longqi-1 HF. However, the DHF exhibits significant differences in the dispersal distance of hydrothermal derived Cu and Zn. Comparatively, the dispersion of these elements within 1–2 km in the DHF show significantly lower contents in Cu than in the Dragon Horn area (Liao et al., 2018). Former studies suggested that the spatial distribution of hydrothermal derived elements in sediments can be mainly affected by the following factors (Coogan et al., 2017): (1) the chemical composition of hydrothermal fluid; (2) the physicochemical environment and biological processes within the hydrothermal plume; (3) the bottom flow and topographic environment and; (4) the scale of hydrothermal activity. In general, the topography and chemical composition of the hydrothermal fluids affect the morphological characteristics of the element distribution in the sediment (Cronan, 1983), while the scale of hydrothermal activity affects the overall dispersal distance of elements. In the DHF and Longqi-1 HF, the main factor that determines the differences in spatial distribution of hydrothermal elements might be the physical and chemical environment during plume dispersal.

The DHF, a magmatic-hosted hydrothermal field, is located on the RVA (Yang et al., 2016a), whereas the Dragon Horn area is located near the OCC termination fault and is dominated by magmatic and tectonic processes (Zhao et al., 2013; Tao et al., 2014; Liang et al., 2014). In the Dragon Horn area, the host rock and the heat source are significantly different from that of magmatic-hosted HFs. This geological context seems to be responsible for the higher content of Cu and for the observed geochemical composition features of the adjacent sediments, (e.g., higher Cu/Fe ratios; Daessle et al., 2000; Liao et al., 2018). In addition, in geological contexts similar to the Dragon Horn, where long-lived detachment faults are thought to provide the pathways for hydrothermal circulation, hydrothermal plumes can show signatures derived by the interaction with mantellic rocks, characterized by very high H_2 and CH_4 concentrations relative to hydrothermal plumes from

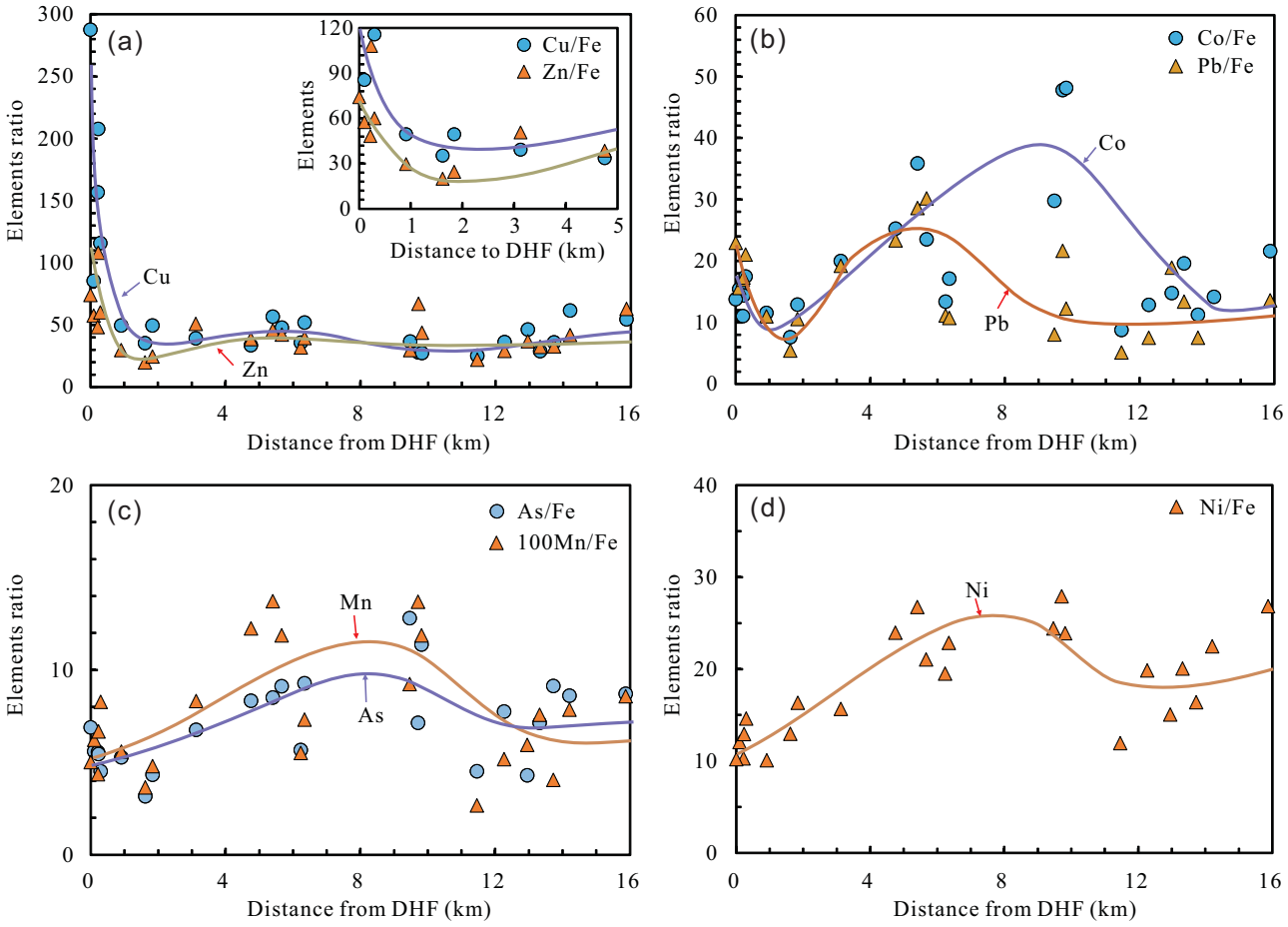

Fig. 8. Cu, Pb, Zn, As, and Mn/Fe ratios in sediments with increasing distances from the DHF. (a) Cu/Fe and Zn/Fe; (b) Co/Fe and Pb/Fe; (c) As/Fe and Mn/Fe; (d) Ni/Fe. Note: Mn/Fe was minus 100 times to be shown on the same scale.

basaltic-hosted systems (Charlou et al., 2002). As a result, this more reduced fluid can retain ions, such as HS^- and S^{2-}, in the hydrothermal plume for a longer time, transporting hydrothermal-derived metals for longer distances that will thus precipitate in sediments in more distal regions. Furthermore, under more reduced conditions, the organic ligands could potentially stabilize the dissolved Cu, Zn, Fe, and Mn in hydrothermal plumes, dispersing these metals to longer distances (Sander and Koschinsky, 2011).

In the DHF, the dispersal distance of hydrothermal Zn is comparable with hydrothermal Cu (DHF Zn: 1.5–2 km; Cu: 1.0–1.5 km; and Figs. 7 and 8) but shows considerably lower concentrations than in the Dragon Horn area (Dragon Horn Zn: 2 km; Cu: 5–6 km; Liao et al., 2018). Differences between the precipitation of Cu and Zn have also been observed in some HFs, where Cu precipitates quicker or slower than Zn (e.g., Mottl and Mcconachy, 1990; Cave et al., 2002; Edmonds and German, 2004; Trocine and Trefry, 1988). Hydrothermal plumes derived from the tectonic-hosted Dragon Horn area are rich in CH_4 and H_2 and are more reducing than those from the volcanic-related DHF. Under these more oxidative conditions, Fe has a higher affinity to react with oxygen and to form oxyhydroxides than Mn (Marbler et al., 2010). As Mn oxidation in the fluids is much slower than Fe, Mn precipitates at higher distances from the source. Additionally, Mn enrichment may

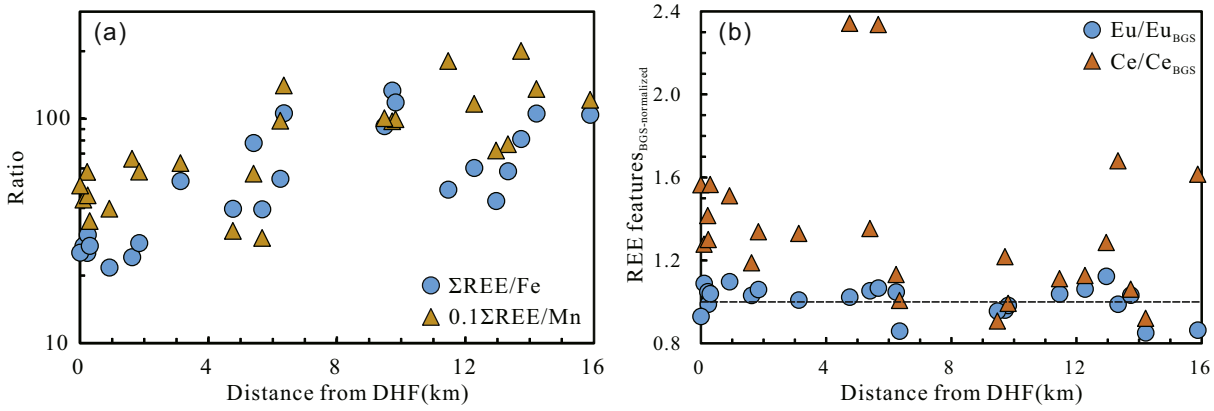

Fig. 9. REY in sediments with increasing distances to the DHF.

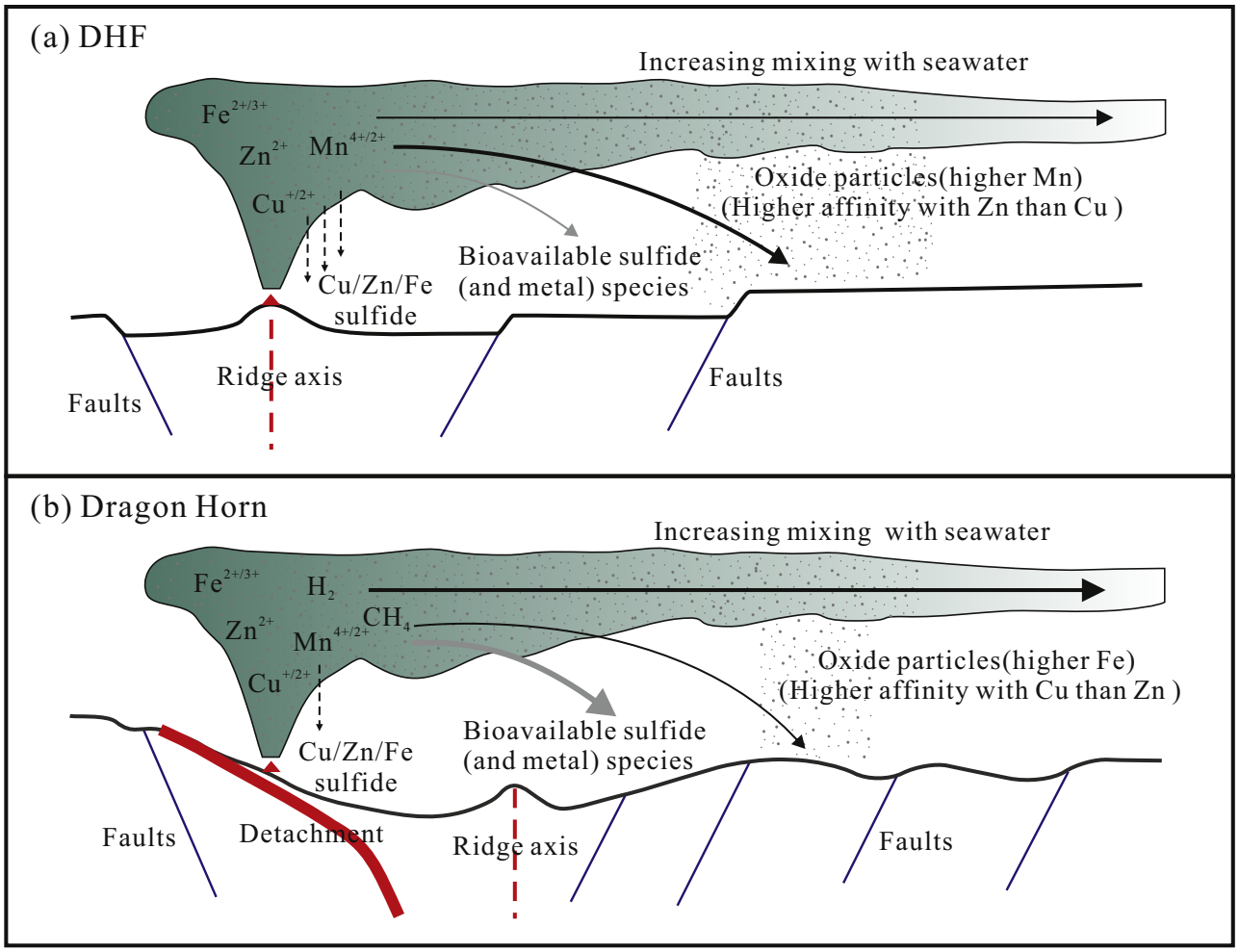

Fig. 10. Diagram showing the dispersion of the hydrothermal plume and consequent precipitation in sediments in (a) the DHF (Duanqiao-1) and (b) Dragon Horn area. The structure of the ridge is modified after Escartin et al. (2008), and hydrothermal fluid–seawater mixing process is modified after Sander and Koschinsky (2011). Hydrothermal plume derived from the tectonic-hosted Dragon Horn area was reduced as a result of high content of CH_4 and H_2 produced by serpentinization, which favors the formation of oxyhydroxide particles rich in Fe during dispersing and mixing with seawater (Marbler et al., 2010). However, the plume derived from the DHF was more oxidizing favors the formation of oxyhydroxide particles rich in Mn. The oxyhydroxide particles enriched in Fe has a higher affinity with Cu than Zn, whereas oxyhydroxide particles enriched in Mn absorbs more Zn than Cu (Koschinsky and Hein, 2003), that probably resulting in the separation of Cu and Zn in the plume.

continue as a result of hydrogenetic precipitation of Mn-rich oxyhydroxides and by biological oxidation. However, the continually oxidizing processes of the plume along the mixing with the oxygenated seawater during plume dispersion will allow the oxidation of Mn at longer distances.

Cu shows a higher affinity with Fe (Koschinsky and Hein, 2003) and an evident fractionation with Zn during hydrothermal plume dispersal (Fig. 10). This results in an increase in the dispersal distance of hydrothermal Cu, as described for other ultramafic-hosted HFs, such as Rainbow (Cave et al., 2002; Edmonds and German, 2004), where Cu disperses to at least 5–6 km away from the vent. It is also consistent with the relatively higher content of Mn in the sediments in the DHF (Fig. 5a) and supported by the higher correlations of Zn with Mn in the DHF than in Dragon Horn (Supplementary Table 1). This suggests that hydrothermal Cu and Zn mainly migrate via absorption to Mn oxyhydroxides in the DHF and to iron oxyhydroxides in the Dragon Horn area. In addition, because Zn only has one oxidation state, it is likely to be most mobile under oxidizing conditions once deposited in the sediment. When sulfides are oxidized to sulfates, Zn will be released to pore waters where it can migrate out of the sediment, thus creating low Zn concentrations under high oxygen conditions (Costa et al., 2018). In addition, Mn oxides are not recycled in the bottom water, where the content of O_2 is $< 5\,\mu M$, whereas Fe oxyhydroxides still behave actively under this condition (Shaw et al., 1990; Emerson and Hedges, 2003; Sun et al., 2018). This process could also lead to desorption and release of scavenged Zn from Fe oxyhydroxides to pore waters in the Dragon Horn area while still stable in the DHF, which is consistent with slightly higher Zn content of the DHF sediments compared with the Dragon Horn area sediments (Fig. 5b).

6. Conclusion

(1) Surface sediments in the DHF are mainly composed of pelagic sediments (carbonate oozes with clay components) with minor contents of basaltic debris, Fe—Mn oxyhydroxides, and hydrothermal components. The hydrothermal content is characterized by an enrichment in Cu, Pb, Zn, and Co in proximal sediments and by a higher Mn and Fe content in the distal ones. Part of the ferromanganese phases from distal areas of the site are of hydrogenetic origin.

(2) Elements/Fe ratios used to characterize the dispersal distances of the hydrothermal derived elements show that Cu precipitates slightly faster than Zn, Fe, and Pb in the proximal sediments, whereas Ni, As, and REY are mainly precipitated in more distal

sediments, probably by being scavenged from the seawater by Mn−Fe oxyhydroxides. Concordantly, Mn-rich oxyhydroxides are mostly precipitated in the distal sediments.

(3) In comparison with the Dragon Horn area (an ultramafic-hosted hydrothermal system), the DHF (a basaltic-hosted hydrothermal system) has a lower dispersion of mineral precipitates around the discharge zone, particularly in relation to the Cu–Zn-rich mineral phases. This may be related to the end-member hydrothermal fluid from DHF being less reduced than in the Dragon Horn area, as a result of rapid oxidation by contact with bottom seawater.

Supplementary data to this article can be found online at https://doi.org/10.1016/j.margeo.2019.105975.

Acknowledgment

This research is funded by the National Key Research and Development Program of China (2018YFC0309902, 2017YFC0306803, 2017YFC0306603, 2017YFC0306800), China Ocean Mineral Resources R&D Association (COMRA) Project (DY135-S1-1-02, 08), Natural Science Foundation of Zhejiang Province (LQ19D060002), Macao Science and Technology Development Fund (FDCT-002/2018/A1), and China Geological Survey (DD20190578). We are grateful for the captains and crews of the DY115-20, DY115-21, DY125-30, DY125-34, DY125-39, DY125-40, and DY135-49 cruises on R/V DayangYihao and R/V Xiangyanghong 10, who contributed to the success of this project. We are also grateful for the constructive comments and suggestions from Editor-in-Chief Gert J. De Lange, Dr. V.Yu. Rusakov and an anonymous reviewer.

References

Baker, E.T., Edmonds, H.N., Michael, P.J., Bach, W., Dick, H., Snow, J.E., Walker, S.L., Banerjee, N.R., Langmuir, C.H., 2004. Hydrothermal venting in magma deserts: the ultraslow-spreading Gakkel and Southwest Indian Ridges. Geochemistry Geophysics Geosystems 5 (8), Q8002.

Baumberger, T., Früh-Green, G.L., Thorseth, I.H., Lilley, M.D., Hamelin, C., Bernasconi, S.M., Okland, I.E., Pedersen, R.B., 2016. Fluid composition of the sediment-influenced Loki's Castle vent field at the ultra-slow spreading Arctic Mid-Ocean Ridge. Geochim. Cosmochim. Acta 187, 156–178.

Boström, K., 1973. The origin and fate of ferromanganoan active ridge sediments. Stockholm. Contributions to Geology 27, 149–243.

Boström, K., Peterson, M.N.A., Joensuu, O., Fisher, D.E., 1969. Aluminum-poor ferromanganoan sediments on active oceanic ridges. Journal of Geophysical Research Atmospheres 74 (12), 3261–3270.

Cannat, M., Rommevaux-Jestin, C., Sauter, D., Deplus, C., Mendel, V., 1999. Formation of the axial relief at the very slow spreading Southwest Indian Ridge (49° to 69°E). Journal of Geophysical Research Atmospheres 104 (B10), 22825–22843.

Cave, R.R., German, C.R., Thomson, J., Nesbitt, R.W., 2002. Fluxes to sediments underlying the Rainbow hydrothermal plume at 36°14′ N on the Mid-Atlantic Ridge. Geochim. Cosmochim. Acta 66 (11), 1905–1923.

Charlou, J.L., Donval, J.P., Fouquet, Y., Jean-Baptiste, P., Holm, N., 2002. Geochemistry of high H2 and CH4 vent fluids issuing from ultramafic rocks at the Rainbow hydrothermal field (36°14′N, MAR). Chem. Geol. 191 (4), 345–359.

Chavagnac, V., German, C.R., Milton, J.A., Palmer, M.R., 2005. Sources of REE in sediment cores from the Rainbow vent site (36 14′ N, MAR). Chem. Geol. 216 (3), 329–352.

Chen, Y.Y., Yu, B.S., Su, X., Yu, M., 2013. Mineralogical and Geochemical Characteristics of the Calcareous Sediments in Southwest Indian Ridge. Geological Science and Technology Information 32 (01), 107–113 (In Chinese with English abstract).

Chen, L., Chu, F.Y., Zhu, J.H., Dong, Y.H., Yu, X., Li, Z.G., Tang, L.M., 2015. Major and trace elements of abyssal peridotites: evidence for melt refertilization beneath the ultraslow-spreading Southwest Indian Ridge (53°E segment). Int. Geol. Rev. 57 (13), 1715–1734.

Coogan, L.A., Attar, A., Mihaly, S.F., Jeffries, M., Pope, M., 2017. Near-vent chemical processes in a hydrothermal plume: insights from an integrated study of the Endeavour segment. Geochemistry Geophysics Geosystems 18 (4), 1641–1660.

Corliss, J.B., Dymond, J., Gordon, L.I., Edmond, J.M., von Herzen, R.P., Ballard, R.D., Green, K., Williams, D., Bainbridge, A., Crane, K., 1979. Submarine thermal springs on the Galapagos Rift. Science 203 (4385), 1073–1083.

Costa, K.M., Anderson, R.F., Mcmanus, J.F., Winckler, G., Middleton, J.L., Langmuir, C.H., 2018. Trace element (Mn, Zn, Ni, V) and authigenic uranium (aU) geochemistry reveal sedimentary redox history on the Juan de Fuca Ridge, North Pacific Ocean. Geochim. Cosmochim. Acta 236, 79–98.

Cronan, D.S., 1983. Metalliferous sediments in the CCOP/SOPAC region of the Southwest Pacific: with particular reference to geochemical exploration for the deposits. UN ESCAP CCOP/SOPAC Technical Bulletin 5, 55.

Cruz, M.I.F.S., 2016. Mineralogy and Geochemistry of Contrasting Hydrothermal Systems on the Arctic Mid Ocean Ridge (AMOR): The Jan Mayen and Loki's Castle Vent Fields. Universidade de Lisboa, pp. 773–785.

Daessle, L.W., Cronan, D.S., Marchig, V., Wiedicke, M., 2000. Hydrothermal sedimentation adjacent to the propagating Valu Fa Ridge, Lau Basin, SW Pacific. Mar. Geol. 162 (2–4), 479–500.

Dias, A.S., Barriga, F.J., 2006. Mineralogy and geochemistry of hydrothermal sediments from the serpentinite-hosted Saldanha hydrothermal field (36 34′ N; 33 26′ W) at MAR. Mar. Geol. 225 (1), 157–175.

Dias, Á., Mills, R.A., Ribeiro da Costa, I., Costa, R., Taylor, R.N., Cooper, M.J., Barriga, F.J.A.S., 2010. Tracing fluid–rock reaction and hydrothermal circulation at the Saldanha hydrothermal field. Chem. Geol. 273, 168–179.

Dick, H.J., Lin, J., Schouten, H., 2003. An ultraslow-spreading class of ocean ridge. Nature 426 (6965), 405–412.

Du, Y.S., Jie, Z., Gu, S.Z., Xu, Y.J., Yang, J.H., 2007. Sedimentary geochemistry of the Cambrian-Ordovician cherts: implication on archipelagic ocean of North Qilian orogenic belt. Sci. China Ser. D Earth Sci. 50 (11), 1628–1644.

Edmonds, H.N., German, C.R., 2004. Particle geochemistry in the Rainbow hydrothermal plume, Mid-Atlantic Ridge. Geochim. Cosmochim. Acta 68 (4), 759–772.

Elderfield, H., Hawkesworth, C.J., Greaves, M.J., Calvert, S.E., 1981. Rare earth element geochemistry of oceanic ferromanganese nodules and associated sediments. Geochim. Cosmochim. Acta 45 (4), 513–528.

Emerson, S., Hedges, J., 2003. Sediment Diagenesis and Benthic Flux. Treatise on Geochemistry. pp. 293–319.

Escartin, J., Smith, D.K., Cann, J., Schouten, H., Langmuir, C.H., Escrig, S., 2008. Central role of detachment faults in accretion of slow-spreading oceanic lithosphere. Nature 455 (7214), 790–795.

Feely, R.A., Lewison, M., Massoth, G.J., Robert Baldo, G., Lavelle, J.W., Byrne, R.H., Von Damm, K.L., Curl, H.C., 1987. Composition and dissolution of black smoker particulates from active vents on the Juan de Fuca Ridge. Journal of Geophysical Research: Solid Earth (1978–2012) 92 (B11), 11347–11363.

Feely, R.A., Trefry, J.H., Massoth, G.J., Metz, S., 1991. A comparison of the scavenging of phosphorus and arsenic from seawater by hydrothermal iron oxyhydroxides in the Atlantic and Pacific Oceans. Deep Sea Research Part A Oceanographic Research Papers 38 (6), 617–623.

General Bathymetric Chart of the Oceans (GEBCO), 2010. GEBCO_08 grid, version 20100927. Br. Oceanogr. Data Cent., Liverpool, U. K.(Available at http://www.gebco.net).

German, C.R., 2003. Hydrothermal activity on the eastern SWIR (50°–70°E): evidence from core-top geochemistry, 1887 and 1998. Geochem. Geophys. Geosyst. 4 (7), 9102.

German, C.R., Hergt, J., Palmer, M.R., Edmond, J.M., 1999. Geochemistry of a hydrothermal sediment core from the OBS vent-field, 21°N East Pacific Rise. Chem. Geol. 155 (1), 65–75.

Hannington, M.D., de Ronde, C.D., Petersen, S., 2005. Sea-floor tectonics and submarine hydrothermal systems. Econ. Geol. 100, 111–141.

Hannington, M.D., Jamieson, J., Monecke, T., Petersen, S., Beaulieu, S., 2011. The abundance of seafloor massive sulfide deposits. Geology 39 (12), 1155–1158.

Hrischeva, E., Scott, S.D., 2007. Geochemistry and morphology of metalliferous sediments and oxyhydroxides from the Endeavour segment, Juan de Fuca Ridge. Geochim. Cosmochim. Acta 71 (14), 3476–3497.

Huang, X., Chen, S., Zeng, Z.G., Pu, X.Q., Hou, Q.H., 2017. The influence of seafloor hydrothermal activity on major and trace elements of the sediments from the South Mid-Atlantic Ridge. J. Ocean Univ. China 16 (1), 1–6.

Hung, J.J., Yeh, H.Y., Peng, S.H., Chen, C.T.A., 2018. Influence of submarine hydrothermalism on sulfur and metal accumulation in surface sediments in the Kueishantao venting field off northeastern Taiwan. Mar. Chem. 198, 88–96.

Jian, H.C., Singh, S.C., Chen, Y.J., Li, J.B., 2017. Evidence of an axial magma chamber beneath the ultraslow-spreading Southwest Indian Ridge. Geology 45 (2), G38351–G38356.

Koschinsky, A., Hein, J.R., 2003. Uptake of elements from seawater by ferromanganese crusts: solid-phase associations and seawater speciation. Mar. Geol. 198 (3), 331–351.

Kuhn, T., Bau, M., Blum, N., Halbach, P., 1998. Origin of negative Ce anomalies in mixed hydrothermal–hydrogenetic Fe–Mn crusts from the Central Indian Ridge. Earth Planet. Sci. Lett. 163 (1–4), 207–220.

Kuhn, T., Burger, H., Castradori, D., Halbach, P., 2000. Volcanic and hydrothermal history of ridge segments near the Rodrigues Triple Junction (Central Indian Ocean) deduced from sediment geochemistry. Mar. Geol. 169 (3), 391–409.

Laurila, T.E., Hannington, M.D., Petersen, S., Garbe-Schoenberg, D., 2014. Trace metal distribution in the Atlantis II Deep (Red Sea) sediments. Chem. Geol. 386, 80–100.

Li, J.B., Jian, H.C., Chen, Y.S.J., Singh, S.C., Ruan, A., Qiu, X.L., Zhao, M.H., Wang, X.G., Niu, X.G., Ni, J.Y., Zhang, J.Z., 2015. Seismic observation of an extremely magmatic accretion at the ultraslow spreading Southwest Indian Ridge. Geophys. Res. Lett. 42 (8), 2656–2663.

Liang, Y.Y., Li, J.B., Li, S.J., Ni, J.Y., Ruan, A.G., 2014. The Magmato-tectonic dynamic model for the Indomed-Gallieni of the central southwest Indian ridge. Chin. J. Geophys. 57 (9), 2993–3005 (In Chinese with English abstract).

Liao, G.H., Zhou, B.F., Liang, C.J., Zhou, H.Y., Ding, T., Yuan, W., Dong, C.M., 2015. Moored observation of abyssal flow and temperature near a hydrothermal vent on the Southwest Indian Ridge. Journal of Geophysical Research Oceans 121 (1), 836–860.

Liao, S.L., Tao, C.H., Li, H.M., Zhang, G.Y., Liang, J., Yang, W.F., 2017. Use of portable X-ray fluorescence in the analysis of surficial sediments in the exploration of hydrothermal vents on the Southwest Indian Ridge. Acta Oceanol. Sin. 36 (7), 66–76.

Liao, S.L., Tao, C.H., Li, H.M., Zhang, G.Y., Liang, J., Yang, W.F., Wang, Y., 2018. Surface

sediment geochemistry and hydrothermal activity indicators in the Dragon Horn area on the Southwest Indian Ridge. Mar. Geol. 398, 22–34.
Ludden, J.N., Thompson, G., 1979. An evaluation of the behavior of the rare earth elements during the weathering of sea-floor basalt. Earth Planet. Sci. Lett. 43 (1), 85–92.
Marbler, H., Koschinsky, A., Pape, T., Seifert, R., Weber, S., Baker, E.T., de Carvalho, L.M., Schmidt, K., 2010. Geochemical and physical structure of the hydrothermal plume at the ultramafic-hosted Logatchev hydrothermal field at 14 degrees 45′ N on the Mid-Atlantic Ridge. Mar. Geol. 271 (3–4), 187–197.
Mcarthur, J.M., Elderfield, H., 1977. Metal accumulation rates in sediments from Mid-Indian Ocean Ridge and Marie Celeste Fracture Zone. Nature 266 (5601), 437–439.
Mottl, M.J., Mcconachy, T.F., 1990. Chemical processes in buoyant hydrothermal plumes on the East Pacific Rise near 21°N. Geochim. Cosmochim. Acta 54 (7), 1911–1927.
Niu, X., Ruan, A., Li, J., Minshull, T.A., Sauter, D., Wu, Z., Qiu, X., Zhao, M., Chen, Y.J., Singh, S., 2015. Along-axis variation in crustal thickness at the ultraslow spreading Southwest Indian Ridge (50°E) from a wide-angle seismic experiment. Geochem. Geophys. Geosyst. 16 (2), 468–485.
Pan, A.Y., Yang, Q.H., Zhou, H.Y., Ji, F.W., Wang, H., Pancost, R.D., 2018. Geochemical impacts of hydrothermal activity on surface deposits at the Southwest Indian Ridge. Deep-Sea Res. I Oceanogr. Res. Pap. 139, 1–13.
Rusakov, V.Y., Shilov, V.V., Ryzhenko, B.N., Gablina, I.F., Roshchina, I.A., Kuz'Mina, T.G., Kononkova, N.N., Dobretsova, I.G., 2013. Mineralogical and geochemical zoning of sediments at the Semenov cluster of hydrothermal fields, 13°31′-13°30′N, Mid-Atlantic Ridge. Geochem. Int. 51 (8), 646–669.
Sander, S.G., Koschinsky, A., 2011. Metal flux from hydrothermal vents increased by organic complexation. Nat. Geosci. 4 (3), 145–150.
Sauter, D., Mendel, V., Rommevaux-Jestin, C., Parson, L.M., Fujimoto, H., Mevel, C., Cannat, M., Tamaki, K., 2004. Focused magmatism versus amagmatic spreading along the ultra-slow spreading Southwest Indian Ridge: evidence from TOBI side scan sonar imagery. Geochemistry Geophysics Geosystems 5, Q10K09.
Shaw, T.J., Gieskes, J.M., Jahnke, R.A., 1990. Early diagenesis in differing depositional environments: the response of transition metals in pore water. Geochim. Cosmochim. Acta 54 (5), 1233–1246.
Sun, Z.L., Cao, H., Yin, X.J., Zhang, X.R., Dong, A.G., Liu, L.P., Geng, W., 2018. Precipitation and subsequent preservation of hydrothermal Fe-Mn oxides in distal plume sediments on Juan de Fuca Ridge. J. Mar. Syst. 187, 128–140.
Tao, C.H., Lin, J., Guo, S.Q., John Chen, Y.S., Wu, G.H., Han, X.Q., German, C.R., Yoerger, D.R., Zhou, N., Li, H.M., Su, X., Zhu, J., 2012. First active hydrothermal vents on an ultraslow-spreading center: Southwest Indian Ridge. Geology 40 (1), 47–50.
Tao, C.H., Li, H.M., Jin, X.B., Zhou, J.P., Wu, T., He, Y.H., Deng, X.M., Gu, C.H., Zhang, G.Y., Liu, W.O., 2014. Seafloor hydrothermal activity and polymetallic sulfide exploration on the southwest Indian ridge. Chin. Sci. Bull. 59 (19), 2266–2276.
Taylor, S.R., Mclennan, S., 1985. The Continental Crust: Its Composition and Evolution. Blackwell Scientific, Oxford, pp. 312.
Trocine, R.P., Trefry, J.H., 1988. Distribution and chemistry of suspended particles from an active hydrothermal vent site on the Mid-Atlantic Ridge at 26°N. Earth Planet. Sci. Lett. 88 (1), 1–15.
Yamamoto, K., 1987. Geochemical characteristics and depositional environments of cherts and associated rocks in the Franciscan and Shimanto Terranes. Sediment. Geol. 52 (1–2), 65–108.
Yang, W.F., 2017. Study of Hydrothermal Mineralization of Duanqiao Hydrothermal Field in Southwest Indian Ridge. Zhejiang University, Hangzhou (In Chinese with English abstract).
Yang, W.F., Tao, C.H., Li, H.M., Liang, J., Liao, S.L., Long, J.P., Ma, Z.B., Wang, L.S., 2016a. $^{230}Th/^{238}U$ dating of hydrothermal sulfides from Duanqiao hydrothermal field, Southwest Indian Ridge. Mar. Geophys. Res. 38, 1–13.
Yang, Y., Rusakov, V.Y., Kuz Mina, T.G., 2016b. Rare earth elements in the ore-bearing sediments of the Krasnov and Semenov hydrothermal fields, Mid-Atlantic Ridge. Geochem. Int. 54 (3), 280–292.
Yang, A.Y., Zhao, T.P., Zhou, M.F., Deng, X.G., 2017. Isotopically enriched N-MORB: a new geochemical signature of off-axis plume-ridge interaction-a case study at 50°28′E, Southwest Indian Ridge. J. Geophys. Res. 122 (1), 191–213.
Yu, Z.H., Li, H.M., Li, M.X., Zhai, S.K., 2018. Hydrothermal signature in the axial-sediments from the Carlsberg Ridge in the Northwest Indian Ocean. J. Mar. Syst. 180, 173–181.
Zeng, Z.G., Ma, Y., Yin, X.B., Selby, D., Kong, F.C., Chen, S., 2015. Factors affecting the rare earth element compositions in massive sulfides from deep-sea hydrothermal systems. Geochemistry Geophysics Geosystems 16 (8), 2679–2693.
Zhao, M., Qiu, X., Li, J., Sauter, D., Ruan, A., Chen, J., Cannat, M., Singh, S., Zhang, J., Wu, Z., Niu, X., 2013. Three-dimensional seismic structure of the Dragon Flag oceanic core complex at the ultraslow spreading Southwest Indian Ridge (49°39′ E). Geochemistry Geophysics Geosystems 14 (10), 4544–4563.